Published in final edited form as:
Neuroimage. 2011 February 1; 54(3): 2079–2085. doi:10.1016/j.neuroimage.2010.10.017.

In vivo Mapping of Brain Myo-Inositol

Mohammad Haris[*,1], **Kejia Cai**[*,1], **Anup Singh**[*,1], **Hari Hariharan**[1], and **Ravinder Reddy**[1]
[1]CMROI, Department of Radiology, University of Pennsylvania, Philadelphia, PA

Abstract

Myo-Inositol (MI) is one of the most abundant metabolites in the human brain located mainly in glial cells and functions as an osmolyte. The concentration of MI is altered in many brain disorders including Alzheimer's disease and brain tumors. Currently available magnetic resonance spectroscopy (MRS) methods for measuring MI are limited to low spatial resolution. Here, we demonstrate that the hydroxyl protons on MI exhibit chemical exchange with bulk water and saturation of these protons leads to reduction in bulk water signal through a mechanism known as chemical exchange saturation transfer (CEST). The hydroxyl proton exchange rate (k=600 Hz) is determined to be in the slow to intermediate exchange regime on the NMR time scale (chemical shift ($\Delta\omega$)>k), suggesting that the CEST effect of MI (MICEST) can be imaged at high fields such as 7T ($\Delta\omega=1.2\times10^3$rad/s) and 9.4T ($\Delta\omega=1.6\times10^3$rad/s). Using optimized imaging parameters, concentration dependent broad CEST asymmetry between ~0.2 to 1.5ppm with a peak at ~0.6ppm from bulk water was observed. Further, it is demonstrated that MICEST detection is feasible in the human brain at ultra high fields (7T) without exceeding the allowed limits on radiofrequency specific absorption rate. Results from healthy human volunteers (N=5) showed significantly higher (p=0.03) MICEST effect from white matter (5.2±0.5%) compared to gray matter (4.3±0.5%). The mean coefficient of variations for intra-subject MICEST contrast in WM and GM were 0.49 and 0.58 respectively. Potential overlap of CEST signals from other brain metabolites with the observed MICEST map is discussed. This noninvasive approach potentially opens the way to image MI *in vivo* and to monitor its alteration in many disease conditions.

Keywords

Brain; Myo-inositol; Exchange rate; Chemical exchange saturation transfer

INTRODUCTION

Myo-Inositol (MI) is one of the most abundant metabolites visible on proton magnetic resonance spectroscopy (^{1}HMRS) of the human brain. MI is a sugar like molecule located mainly in glial cells of the brain, functions as an osmolyte, and its concentration is altered in many brain disorders (Brand et al., 1993). During periods of osmotic stress, the osmotic balance is preserved by regulation of MI transport across the plasma membrane. MI is a key

Address for Correspondence Ravinder Reddy, PhD Center for Magnetic Resonance and Optical Imaging (CMROI) Department of Radiology University of Pennsylvania B1 Stellar-Chance Laboratories 422 Curie Boulevard Philadelphia, PA 19104-6100 Tel: (215) 898-2045 Fax: (215) 573-2113 ravi@mail.mmrrcc.upenn.edu.
*M.H. K.C. and AS share equal authorship in the manuscript.

precursor of membrane phospho-inositides and phospholipids and it is also involved in cell membrane and myelin sheet structures. Increased membrane turnover or damage to myelin sheets can result in increased concentrations of free MI.

MI is considered to be a glial marker, and an increase in its content is believed to represent glial proliferation (Brand et al., 1993). Elevated MI levels have been observed in Alzheimer's disease, gliomatosis cerebri, diabetes mellitus, recovering hypoxia, progressive multifocal leukoencephalopathy, systemic lupus erythematosus, familial hemiplegic migraine, in some patients with canavan disease, and in multiple sclerosis (Axford et al., 2001; Dichgans et al., 2005; Kapeller et al., 2005; Katz-Brull et al., 2004; Kreis and Ross, 1992; Macri et al., 2006; Miller et al., 1993; Saraf-Lavi et al., 2003). Further, decreased brain levels of MI were observed in chronic hepatic and hypoxic encephalopathies, stroke, acute thyrotoxic Graves' disease, toxoplasmosis, cryptococcosis, and lymphoma (Elberling et al., 2003; Kinoshita and Yokota, 1997; Laubenberger et al., 1997). Castillo et al. measured the MI concentration in different grades of brain tumors and suggested its role in grading of brain tumors (Castillo et al., 2000).

Currently, ^{1}HMRS is the method of choice to quantify MI *in vivo*. On ^{1}HMRS, MI is usually assigned to the peak present at 3.56ppm. Using MRS, absolute quantification of MI both in gray and white matter has been performed (Wijnen et al.). While some of the studies have shown similar concentration of MI in gray and white matter (Oz et al., 2005; Tkac et al., 2009) and the other using quantitative MR spectroscopy have found higher MI concentrations in the white matter than the gray matter (Minati et al., 2010; Parnetti et al., 1997; Schweinsburg et al., 2003). However, quantification of MI using MRS is limited to low spatial resolution and currently no generally applicable methods for direct MI imaging are available. High-resolution imaging may enable spatial mapping of MI in a multitude of brain disorders related to changes in MI concentration. Given the potential utility of MI and the limitations of currently available approaches, a robust noninvasive imaging method with high spatial resolution for the measurement of MI is highly desirable.

The technique based on the transfer of saturated magnetization from exchangeable protons to bulk water during the irradiation of exchanging spins is commonly known as chemical exchange saturation transfer (CEST) (Forsen and Hoffman, 1963; Sherry and Woods, 2008; Ward et al., 2000; Woessner et al., 2005) and has been used earlier to study different metabolites. Labile amide proton (–NH) exchange with bulk water was exploited to map pH changes in tissues (Ward and Balaban, 2000; Zhou et al., 2003) as well as the protein content in the brain (Jones et al., 2006), while –OH exchange was used to measure the proteoglycan concentration in cartilage (Ling et al., 2008) as well as glycogen concentration changes in the liver (van Zijl et al., 2007).

Here, for the first time, the high-resolution spatial mapping of MI based chemical exchange saturation transfer (MICEST) of –OH protons residing on MI with bulk water is shown. The pH and concentration dependent MICEST effect is demonstrated on known phantoms. The feasibility of measuring MICEST on healthy human brains *in vivo* on a 7T ultra high magnetic field MRI scanner is investigated. Potential overlap with other metabolites and issues related to the quantification of MICEST *in vivo* are discussed.

MATERIALS AND METHODS

CEST Technique

When two nuclear spins with a distinct chemical shift difference, $\Delta\omega$, are in the slow to intermediate exchange regime ($\Delta\omega > k$ *(exchange rate constant)*), frequency selective radiofrequency saturation of one of the spins will lead to simultaneous decrease in the

magnetization of the unsaturated spin due to chemical exchange of the saturated magnetization. This effect is termed as CEST. The saturation transfer magnetization is then imaged to detect the CEST effect from the saturated nuclear spin.

In implementing this method *in vivo*, and interpreting the results the following two key issues have to be addressed:(i) the direct saturation of water and the background magnetization transfer effect in biological tissues;(ii) the amplitude and duration of the saturation pulse and efficiency of saturation. To account for the first, two images are acquired; one with saturation at the resonance frequency of exchanging spin(s) and the other at the equal frequency offset difference on the other side of the bulk water peak and then compute the difference as CEST asymmetry ($CEST_{asym}$) ratio, which provides the CEST effect of the source spins. This is given by Equation [1],

$$CEST_{asym}(\Delta\omega) = \frac{M_{sat}(-\Delta\omega) - M_{sat}(\Delta\omega)}{M_0} \quad [1]$$

where M_0 is the equilibrium magnetization when saturation frequency is set far from the water resonance, such as 20ppm down field of the water resonance, M_{sat} ($\pm\Delta\omega$) are the magnetizations obtained with saturation at a `+' or `−' $\Delta\omega$ offset of the water resonance. The role of amplitude and duration of the saturation pulse can be incorporated into a general solution of a two-site exchange model in the presence of RF saturation as shown in Equation [2] (McMahon et al., 2006; van Zijl et al., 2007; Woessner et al., 2005)

$$CEST_{asym}(\Delta\omega) = \frac{k\alpha f}{R_{1w}+kf}\left[1 - e^{-(R_{1w}+kf)t_{sat}}\right] \quad [2]$$

where k is exchange rate (s^{-1} or Hz), α is the factor that accounts for suboptimal saturation with 1 describing complete saturation (at high enough B_1 amplitude of saturation pulse). For MI CEST imaging, f =n[MI]/2[H_2O] is the fraction of exchangeable protons on MI (n=6 for six –OH), R_{1w} (=$1/T_{1w}$) is the longitudinal relaxation rate of water protons and t_{sat} is the length of the of the saturation pulse. MI $CEST_{asym}$ contrast is referred to as MICEST.

CEST MR Spectroscopy at 9.4T

All the spectroscopic experiments were performed on 9.4 T vertical bore scanner (Inova; Varian, Palo Alto, CA) in 5 mm NMR tubes using 5 mm radiofrequency (RF) probe at room temperature.

To explore the presence of exchangeable protons in MI (Sigma Aldrich, USA), 200 mM phantoms of MI solutions were prepared in distilled water. The pH was adjusted to 6.0 and 7.0 with 1N HCl/NaOH. ^{1}H-spectroscopy of both MI solutions and distilled water were performed with a single pulse acquisition (TR=2second, number of averages = 128).

The exchange rate was calculated from the 10mM MI solution at pH 7.0. Three spectra at +20ppm and ±0.6ppm were acquired with varying B_1 (from 90 Hz to 1.2 KHz), and varying duration from 0 to 6 seconds. The MICEST contrast was calculated for each B_1 and duration. As B_1 increases, MICEST contrast increases and reaches a maximum value ($MICEST_{max}$) and then decreases when B_1 is too high. The $MICEST_{max}$ value obtained with sufficient B_1 along with appropriate duration to accomplish complete saturation was used for the calculation of exchange rate. T_{1w} of the solution was also quantified from the inversion recovery spectrum experiments by varying inversion time (TI) from 50ms to 6s.

The exchange rate was calculated using Equation 3, which is obtained by rearranging Equation [2] as described previously (Sun et al., 2008).

$$k = \frac{MICEST_{\max}}{1 - MICEST_{\max}} * \frac{1}{f * T_{1w}} \quad [3]$$

CEST Imaging on 7.0 T whole body MR scanner

MI solutions with different concentrations (2, 4, 6, 8, 10 and 12mM, pH=7.4) were prepared in small glass tubes (1.5 cm diameter) and immersed in a beaker containing PBS. CEST images from these phantoms were acquired by using a single channel circular polarized transmit-receive head coil on a Siemens whole-body 7.0T clinical MR Scanner (Siemens medical systems, Malvern, PA). A new pulse sequence was designed for selective saturation pulse followed by a segmented RF spoiled gradient echo readout sequence. An optimized saturation pulse train with 50, 75 and 100 Hanning windowed rectangular pulses of 100ms duration each with a 200 μs delay between them was used. The total repetition time of the sequence was adjusted to stay within RF specific absorption rate (SAR) limits. The sequence parameters were: slice thickness = 5mm, GRE flip angle=10°, GRE readout TR=5.6ms, TE =2.7 ms, field of view =120*120 mm, matrix size =192*192, and one saturation pulse and 64 acquired segments every 16s. Three CEST images were collected using different saturation pulse durations (4s, 6s, and 10s) and with different peak B_1 (50 Hz, 75Hz, and 100 Hz) at ±0.6ppm and +20ppm. The total imaging time was about 15minutes.

In addition, Z-spectra from the same phantoms as well as PBS were acquired over a ±3.0ppm range relative to the bulk water resonance frequency in steps of 0.1ppm using the same imaging parameters. Z-spectral data was corrected for B_o and B_1 inhomogeneity and normalized with 20ppm data.

To evaluate the contribution of other major metabolites i.e glucose (Glc), glycogen (Gly), creatine (Cr), glutamate (Glu) and γ- amino butyric acid (GABA) to the MICEST, we made solution of each metabolite (pH 7.4) in the range of their physiological concentration [Glc (3mM), Gly (3mM), Cr (10mM), Glu (10mM), GABA (2mM) and MI (10mM) (Sigma Aldrich, USA)] and performed the CEST imaging using similar imaging parameters as described above with varying saturation pulse B_1.

To evaluate the CEST contrast dependency on the viscosity and temperature, we performed the CEST imaging of 10mM MI in three different viscous media i.e. 1%, 2% and 3% agarose (Sigma Aldrich, USA), and at two different temperatures (25° C and 37° C), using the same imaging parameters as mentioned above.

MICEST imaging was also performed *in vivo* on five healthy volunteers (age: 27–35) using the same transmit-receive head coil and imaging protocols as in the case of phantom MICEST imaging. Only the field of view =240*240 and matrix size=128*128were different. The CEST imaging was performed at peak B_1 of 75Hz and 6s saturation pulse duration. Brain Z-spectra were acquired from CEST images with varying saturation frequency from −1.5ppm to +1.5ppm and 0.05ppm steps and the signals were normalized with +20ppm image. The total imaging time including B_o and B_1 mapping was around 35 minutes. Informed consent from each volunteer was obtained after explaining the study protocol. The Institutional Review Board of University of Pennsylvania approved all study protocols.

B_0 and B_1 Maps

B_0 and B_1 inhomogeneities in the brain slice were corrected using B_0 and B_1 maps generated from the same slice. Using the gradient echo images collected at different

TE=2.11, 3.17, 4.23, 5.29, 6.35 and 14.8 ms the B_0 map was derived by linearly fitting the accumulated pixel phase $\Delta\theta_0$ following phase unwrapping against the echo time differences (ΔTE).

$$B_0 = \frac{\Delta\theta_0}{\Delta TE} \quad [4]$$

For B_1 map, two images were obtained using preparation square pulses with flip angles I_1=30° andI_2=60° (pulse duration τ=1 ms) followed by a spoiler gradient. Flip angle (I) maps were generated by solving Equation [5],

$$\frac{\cos(I_2)}{\cos(I_1)} = \frac{S(I_2)}{S(I_1)} \quad [5]$$

where $S(I_1)$ and $S(I_2)$ denote pixel signals in an image with preparation flip angle I_1 and I_2 respectively. Using the relation $B_1 = I / 360\tau$, the B_1 map was generated.

B_0 and B_1 Corrections

B_0 map and multiple CEST data, acquired in the neighborhood of ±0.6ppm at steps of 0.05ppm, was used to generate corrected MICEST images (±0.6ppm) using procedure similar to that described previously (Kim et al., 2009). Specifically, MICEST data obtained from 0 to ±1.2ppm with a step size of 0.05ppm were interpolated using cubic spline to generate CEST data in step size of 0.0125ppm. Each voxel value of ±0.6ppm image was replaced by neighborhood MICEST data (0 to ±1.2ppm) value according to amount of shift in frequency as measured from the B_0 map. No change takes place to the voxels of ±0.6ppm images with frequency shift <0.0125ppm. The corrected ±0.6ppm images were then used for computing the final MICEST map.

MICEST contrasts were normalized with B_1/B_{1ref} to correct B_1 inhomogeneity. RF pulse amplitude for 30° flip angle was used as B_{1ref}.

Image Processing

All image processing and data analysis was performed using MATLAB (version 7.5, R2007b). Original MICEST images (–0.6 and +0.6ppm) were B_0 corrected and MICEST contrast was calculated from the Equation [1] and B_1 corrected. MICEST contrast was color coded onto one original image acquired with offset of 0.6ppm. Segmentation of white and gray matter was performed using a combination of standard fast spin echo T2 and proton density weighted images.

Student t-test was performed for MICEST contrast between white and gray matter to see any statistically significant difference. Coefficient of variation of MICEST from each volunteer was calculated as the standard deviation over mean.

RESULTS

High-resolution ^{1}H NMR spectra of MI (pH 6.0 and pH 7.0, 200 mM) and distilled water (pH 6.0) are shown in figure 1. ^{1}H NMR spectrum of MI showed three peaks downfield to the bulk water proton resonance. The spectrum also showed –CH resonances from MI upfield to the water proton resonance. At a pH of 6.0 (Fig. 1A), the MI –OH peaks were narrower compared to that at pH 7.0 (Fig. 1B) due to slower exchange rate (Sun and Sorensen, 2008). The distilled water spectrum showed no peak other than water (Fig. 1C).

Based on this initial finding, we assigned the three peaks present downfield to the bulk water were from the MI-OH resonances.

Figure 2 shows the Z-spectra of MI at different concentrations as well as PBS at a pH of 7.4. The MI Z-spectra showed a broad CEST peak centered at ~0.6ppm downfield to the bulk water resonance, demonstrating that the –OH peaks of MI are the exchangeable groups responsible for creating a broad CEST effect spanning from ~0.2ppm to 1.5ppm. The PBS Z-spectra showed no CEST effect (Fig. 2). CEST asymmetry curves obtained from the Z-spectra clearly demonstrated the broader CEST effect centered at ~0.6ppm (Fig. 2B).

The T1 value measured from 10 mM MI solution at 9.4 T was 2.7s. The exchange rate (*k*) was calculated to be around 600Hz using the Equation [3].

MICEST imaging of MI phantoms at varying concentrations (2, 4, 6, 8, 10 and 12mM, pH=7.4) was also performed on a 7T whole body scanner. The subtracted images showed signal only from the inner chambers containing MI (Fig. 3A). Due to symmetric saturation related to the bulk water resonance, no CEST contrast was observed from the outer chambers containing PBS. Figure 3B shows MI CEST contrast as a function of MI concentrations. This demonstrates that the CEST effect increased with increasing MI concentration, indicating that the CEST effect of MI can serve as an index of its concentration. In figure 3C, the MICEST contrast from 10mM MI solution at three different B_1fields (50 Hz, 75Hz and 100Hz) and saturation pulse durations (4s, 6s and 10s) are shown.

Figure 4 shows the CEST effect from the major brain metabolites at their physiological concentrations (Glc 3mm, Gly 3mM, Glu 10mM, GABA 2mM, Creatine 10mM, MI 10mM). At peak B_1 of 75Hz and 6seconds saturation pulse duration only MI shows predominant CEST contrast with negligible contributions from other metabolites.

Figure 5 shows results for the same concentration of MI (10mM) in different viscous media (1%, 2%, and 3% agarose). We observed that the MICEST contrast was higher in the medium with the 1% followed by the2% and 3% agarose. Increasing the temperature to 37 C also changed the MICEST contrast, which was higher in the medium with 1% agarose (Fig. 5B).

To evaluate whether MI detection is feasible in the brain, we performed the MICEST experiment on the human brain on a 7T clinical scanner. After application of saturation pulses at ±0.6ppm, a relative difference in the water signal was observed similar to the phantom shown in figure 3. To correct for the B_0 and B_1 variations in the brain image, we obtained B_0 and B_1 maps on the same imaging slice shown in figures 6B and 6C. After shimming of the main magnetic field we were able to achieve a fairly uniform B_0 field (<0.3ppm) across the brain image. Similarly, the B_1 map shows small variation across most area of the brain (<30% of reference B_1 or B_{1ref}). MICEST map from an axial slice of human brain is shown in figure 6D. MICEST maps from segmented white and gray matter of the same axial brain slice are shown in figures 6E and 6F. Overall, white matter regions exhibited significantly higher (p=0.03) MICEST than the gray matter regions. Figure 7 shows the CEST asymmetry curves obtained from gray and white matter regions of healthy human brain. These curves showed the maximum CEST contrast at around 0.6ppm.

Table 1 shows average MICEST values and coefficient of variation (CV) from white and gray matter regions of healthy volunteers.

DISCUSSION

The high-resolution NMR spectra showed three MI-OH peaks downfield to the bulk water resonance at pH6.0, which broadened at pH7.0. This may be due to the pH dependent change in the exchange rate, which is known to be decreased at low pH (Sun et al., 2008). Z-spectra acquired with MI solutions at varying concentrations showed a broad CEST effect (0.1ppm to 1.2ppm) centered at ~0.6ppm and indicate that the peaks present downfield to the bulk water are due to exchangeable groups on MI.

At physiological pH 7.4 the exchange rate (k) was determined to be ~600 Hz. Compared to the chemical shift difference both at 9.4T ($\Delta\omega=1.6\times10^3$ rad/s) and 7T ($\Delta\omega=1.2\times10^3$ rad/s) the exchange rate of MI -OH proton is in slow to intermediate exchange rate and satisfies the condition ($\Delta\omega>k$).

For measurement of k based on the equation [3], sufficient B_1andpulse duration is prerequisite for complete saturation. In the current study, this condition was met at 200 Hz with 6s duration.

We demonstrated the feasibility of implementing the MICEST experiment on a 7T whole-body MR scanner by performing the experiments on different concentrations of MI solution. While we observed the concentration dependent CEST contrast from different concentrations of MI solution, no contrast was observed from PBS alone, indicating symmetric saturation of the bulk water resonance. It is worth comparing the potential sensitivity advantage of CEST in detecting MI compared to traditional MRS measurement based on aliphatic protons (-CH). Assuming that average brain MI concentration is 8mM, the proton signal from a single –CH group is detected as 8mM. On the other hand, from Fig. 3, 8mM MI leads to a ~6% CEST effect from the six –OH protons. This implies that ~6.6M decrease in water proton concentration from 110M. In essence, the CEST provides a >200 fold amplification of MI under physiological conditions.

The presence of six exchangeable –OH protons in MI makes it a more appropriate endogenous CEST agent. A CEST effect has been previously reported from –OH protons on Glc and Gly (van Zijl et al., 2007). While the Z-spectra from glucose showed three CEST peaks between1–2ppm downfield to the bulk water, glycogen Z-spectra showed a CEST peak at 1ppm downfield to bulk water (van Zijl et al., 2007). The reasonable chemical shift difference (0.3–1.3ppm) between the MI–OH and Glc –OH protons minimizes the probability of overlap of CEST effects between these two metabolites. The normal Glc and Gly concentration in brain is ~2–4.0mM (Choi and Gruetter, 2003; Criego et al., 2005) and it was shown that at physiological pH, CEST effect at these concentrations is negligible (van Zijl et al., 2007).

The other major metabolites in the brain with significant concentrations are: N-acetyl aspartate (NAA), choline (Cho), Cr, Glu, GABA and glutamine (Gln). Of these metabolites, Cho does not have any exchangeable protons to provide CEST. Amide proton on NAA is expected to resonate beyond 3.0ppm and at the physiological pH we did not observe any CEST effect from it. At the physiological pH, amine protons from Gln do not exhibit appreciable CEST effect. Cr, GABA and Glu with their –NH2 protons exhibit CEST effect at 2.0ppm, 2.75ppm and 3ppm, respectively. The Cr and Glu concentration in the brain is around 10mM while the concentration of GABA is around 2mM. To evaluate any CEST effect from these metabolites at 0.6ppm due to the exchange broadening, we made solution of these metabolites in their respective concentration i.e. Cr (10mM), Glu (10mM) and GABA (2mM), Glc (3 mM), Gly (3 mM) along with MI (10mM) and immersed in a large beaker containing PBS. At 75Hz B_1 and 6s duration of saturation pulse we observed predominant CEST effect from MI and negligible contribution from other metabolites.

However, increasing the B_1 (>75Hz) not only increases the MICEST contrast but also leads to measurable CEST effect from other metabolites (data not shown). This demonstrates that the choice of 75Hz B_1 and ~6s long saturation pulse, leads to minimal contamination from other metabolites to MICEST contrast.

In vivo Human Brain Imaging

It is possible that the observed MICEST effect in human brain may be affected by MI concentration, viscosity as well as temperature. As it is well known, temperature and viscosity changes are reflected in the exchange rate. Although we used agarose to change the viscosity it does not mimic the true physiological condition. Under physiological condition the temperature is constant and viscosity varies between white matter, gray matter and CSF. In general, white matter has higher viscosity as compared to the gray matter and CSF. Given that higher viscosity leads to lower CEST (based on the results from agarose phantoms), if the viscosity is the factor that contributing to the MICEST then the observed MICEST in the white matter should be lower than that of the gray matter; which is not the case. Hence, the difference in MICEST in vivo may be predominantly due to difference in MI concentration and contributions from viscosity and from other variables, if any, may be minor. These observations are supported by some of the previous MRS studies that have shown higher MI concentration in white matter than in gray matter regions. The CEST asymmetry curves from the gray and white matter showed a broad peak centered at ~0.6ppm (Fig. 6F).

In this study, we observed statistically significant difference ($p=0.03$) of MICEST from white and gray matter. The average MICEST from white matter ($n=5$) is 5.2±0.5% and from gray matter is ~4.3±0.5%, which are consistent with the reported difference between MRS derived white and gray matter MI levels (Minati et al., 2010; Parnetti et al., 1997; Schweinsburg et al., 2003). This is also supported by immunohisto-pathological studies that have shown significantly higher glial cells density in white matter than in gray matter (Mittelbronn et al., 2001; Savchenko et al., 1997). On human brain ~20–30% higher microglial cells were observed in white matter compared to gray matter (Mittelbronn et al., 2001). However, as this is a preliminary study on a limited number of subjects, an extensive human study is required to draw firm conclusions on the gray and white matter variations of MICEST.

Since the CEST effect is highly dependent on local B_0 and B_1 homogeneity, in this study, B_0 and B_1 maps were used to effectively correct MICEST maps. It is worthwhile discussing the effects of suboptimal B_0 correction to MICEST. B_0 inhomogeneity potentially leads to the shift in CEST asymmetry curve and also affects the magnitude of MICEST observed at ~0.6ppm. Similarly B_1 inhomogeneity causes inaccurate MICEST values which can be corrected with a linear model for the B_1 variations reported in this paper. Overall, a robust B_0 and B_1 correction is necessary to quantify MICEST.

In this study, we are able to detect an average 5% MICEST from human brain, which will enable the detection of changes in the MI concentration due to pathological changes.

The higher spatial resolution of CEST imaging will provide improved diagnosis and prognosis efficacy in all the pathologies with altered MI. In this study, while we used very small B_1 (75Hz) and 6s pulse duration for MICEST imaging saturation pulse power, duration, and pulse shapes could still be optimized to improve the observed CEST effect.

SUMMARY

In conclusion, for the first time, we demonstrated that the brain MI can be detected using the MICEST method in which saturation of –OH groups on MI contribute to the bulk water

signal change. The magnitude of the MICEST contrast is highly dependent on the pH, MI concentration and saturation pulse parameters. Further, using phantom experiments, we showed that the contributions to MICEST from other metabolites from the brain are negligible. Hence, in this study, we attributed the *in vivo* observed different MICEST contrast from gray and white matter from brain is predominantly due to the endogenous MI. While this may be likely, an unequivocal confirmation that the *in vivo* observed results are from endogenous MICEST require endogenous or exogenous modulation of the MI and resulting MICEST data. Nevertheless, the results could be still used for relative measurement of changes in brain MI levels. Therefore, high resolution mapping of MI would be a useful technique for monitoring different disease states, their progression, and efficacy of treatment, and may provide a new disease biomarker in the future.

Research Highlights

- Hydroxyl protons on Myo-Inositol (MI) exhibit chemical exchange saturation transfer (CEST) effect
- CEST effect of MI (MICEST) can be imaged at high field MRI scanner
- The magnitude of the MICEST contrast is highly dependent on the pH, MI concentration and saturation pulse parameters
- It is demonstrated that MICEST detection is feasible in the human brain at ultra high fields (7T) without exceeding the allowed limits on radiofrequency specific absorption rate.

Acknowledgments

The authors thank Drs. Weixia Liu and Steve Pickup for their technical assistance in using the 9.4T research scanners.

Funding This work was performed at an NIH supported resource with funding from P41RR02305.

REFERENCES

Axford JS, Howe FA, Heron C, Griffiths JR. Sensitivity of quantitative (1)H magnetic resonance spectroscopy of the brain in detecting early neuronal damage in systemic lupus erythematosus. Ann Rheum Dis 2001;60:106–111. [PubMed: 11156541]

Brand A, Richter-Landsberg C, Leibfritz D. Multinuclear NMR studies on the energy metabolism of glial and neuronal cells. Dev Neurosci 1993;15:289–298. [PubMed: 7805581]

Castillo M, Smith JK, Kwock L. Correlation of myo-inositol levels and grading of cerebral astrocytomas. AJNR Am J Neuroradiol 2000;21:1645–1649. [PubMed: 11039343]

Choi IY, Gruetter R. In vivo 13C NMR assessment of brain glycogen concentration and turnover in the awake rat. Neurochem Int 2003;43:317–322. [PubMed: 12742075]

Criego AB, Tkac I, Kumar A, Thomas W, Gruetter R, Seaquist ER. Brain glucose concentrations in healthy humans subjected to recurrent hypoglycemia. J Neurosci Res 2005;82:525–530. [PubMed: 16235252]

Dichgans M, Herzog J, Freilinger T, Wilke M, Auer DP. 1H-MRS alterations in the cerebellum of patients with familial hemiplegic migraine type 1. Neurology 2005;64:608–613. [PubMed: 15728280]

Elberling TV, Danielsen ER, Rasmussen AK, Feldt-Rasmussen U, Waldemar G, Thomsen C. Reduced myo-inositol and total choline measured with cerebral MRS in acute thyrotoxic Graves' disease. Neurology 2003;60:142–145. [PubMed: 12525741]

Forsen S, Hoffman RA. Study of moderately rapid chemical exchange reactions by means of nuclear magnetic double resonance. J. Chem. Phys 1963;39:2892–2901.

Jones CK, Schlosser MJ, van Zijl PC, Pomper MG, Golay X, Zhou J. Amide proton transfer imaging of human brain tumors at 3T. Magn Reson Med 2006;56:585–592. [PubMed: 16892186]

Kapeller P, Ropele S, Enzinger C, Lahousen T, Strasser-Fuchs S, Schmidt R, Fazekas F. Discrimination of white matter lesions and multiple sclerosis plaques by short echo quantitative 1H-magnetic resonance spectroscopy. J Neurol 2005;252:1229–1234. [PubMed: 15895306]

Katz-Brull R, Lenkinski RE, Du Pasquier RA, Koralnik IJ. Elevation of myoinositol is associated with disease containment in progressive multifocal leukoencephalopathy. Neurology 2004;63:897–900. [PubMed: 15365144]

Kim M, Gillen J, Landman BA, Zhou J, van Zijl PC. Water saturation shift referencing (WASSR) for chemical exchange saturation transfer (CEST) experiments. Magn Reson Med 2009;61:1441–1450. [PubMed: 19358232]

Kinoshita Y, Yokota A. Absolute concentrations of metabolites in human brain tumors using in vitro proton magnetic resonance spectroscopy. NMR Biomed 1997;10:2–12. [PubMed: 9251109]

Kreis R, Ross BD. Cerebral metabolic disturbances in patients with subacute and chronic diabetes mellitus: detection with proton MR spectroscopy. Radiology 1992;184:123–130. [PubMed: 1319074]

Laubenberger J, Haussinger D, Bayer S, Gufler H, Hennig J, Langer M. Proton magnetic resonance spectroscopy of the brain in symptomatic and asymptomatic patients with liver cirrhosis. Gastroenterology 1997;112:1610–1616. [PubMed: 9136840]

Ling W, Regatte RR, Navon G, Jerschow A. Assessment of glycosaminoglycan concentration in vivo by chemical exchange-dependent saturation transfer (gagCEST). Proc Natl Acad Sci U S A 2008;105:2266–2270. [PubMed: 18268341]

Macri MA, D'Alessandro N, Di Giulio C, Di Iorio P, Di Luzio S, Giuliani P, Bianchi G, Esposito E. Regional changes in the metabolite profile after long-term hypoxia-ischemia in brains of young and aged rats: a quantitative proton MRS study. Neurobiol Aging 2006;27:98–104. [PubMed: 16298245]

McMahon MT, Gilad AA, Zhou J, Sun PZ, Bulte JW, van Zijl PC. Quantifying exchange rates in chemical exchange saturation transfer agents using the saturation time and saturation power dependencies of the magnetization transfer effect on the magnetic resonance imaging signal (QUEST and QUESP): Ph calibration for poly-L-lysine and a starburst dendrimer. Magn Reson Med 2006;55:836–847. [PubMed: 16506187]

Miller BL, Moats RA, Shonk T, Ernst T, Woolley S, Ross BD. Alzheimer disease: depiction of increased cerebral myo-inositol with proton MR spectroscopy. Radiology 1993;187:433–437. [PubMed: 8475286]

Minati L, Aquino D, Bruzzone MG, Erbetta A. Qunatitation of normal metabolite concentrations in six brain regions by in vivo 1H MR sepctroscopy. J Med Phys. 2010 EPub ahead of print.

Mittelbronn M, Dietz K, Schluesener HJ, Meyermann R. Local distribution of microglia in the normal adult human central nervous system differs by up to one order of magnitude. Acta Neuropathol 2001;101:249–255. [PubMed: 11307625]

Oz G, Tkac I, Charnas LR, Choi IY, Bjoraker KJ, Shapiro EG, Gruetter R. Assessment of adrenoleukodystrophy lesions by high field MRS in non-sedated pediatric patients. Neurology 2005;64:434–441. [PubMed: 15699371]

Parnetti L, Tarducci R, Presciutti O, Lowenthal DT, Pippi M, Palumbo B, Gobbi G, Pelliccioli GP, Senin U. Proton magnetic resonance spectroscopy can differentiate Alzheimer's disease from normal aging. Mech Ageing Dev 1997;97:9–14. [PubMed: 9223122]

Saraf-Lavi E, Bowen BC, Pattany PM, Sklar EM, Murdoch JB, Petito CK. Proton MR spectroscopy of gliomatosis cerebri: case report of elevated myoinositol with normal choline levels. AJNR Am J Neuroradiol 2003;24:946–951. [PubMed: 12748099]

Savchenko VL, Nikonenko IR, Skibo GG, McKanna JA. Distribution of Microglia and Astrocytes in Different Regions of the Normal Adult Rat Brain. Neurophysiology 1997;29:431–441.

Schweinsburg BC, Alhassoon OM, Taylor MJ, Gonzalez R, Videen JS, Brown GG, Patterson TL, Grant I. Effects of alcoholism and gender on brain metabolism. Am J Psychiatry 2003;160:1180–1183. [PubMed: 12777281]

Sherry AD, Woods M. Chemical exchange saturation transfer contrast agents for magnetic resonance imaging. Annu Rev Biomed Eng 2008;10:391–411. [PubMed: 18647117]

Sun PZ, Benner T, Kumar A, Sorensen AG. Investigation of optimizing and translating pH-sensitive pulsed-chemical exchange saturation transfer (CEST) imaging to a 3T clinical scanner. Magn Reson Med 2008;60:834–841. [PubMed: 18816867]

Sun PZ, Sorensen AG. Imaging pH using the chemical exchange saturation transfer (CEST) MRI: Correction of concomitant RF irradiation effects to quantify CEST MRI for chemical exchange rate and pH. Magn Reson Med 2008;60:390–397. [PubMed: 18666128]

Tkac I, Oz G, Adriany G, Ugurbil K, Gruetter R. In vivo 1H NMR spectroscopy of the human brain at high magnetic fields: metabolite quantification at 4T vs. 7T. Magn Reson Med 2009;62:868–879. [PubMed: 19591201]

van Zijl PC, Jones CK, Ren J, Malloy CR, Sherry AD. MRI detection of glycogen in vivo by using chemical exchange saturation transfer imaging (glycoCEST). Proc Natl Acad Sci U S A 2007;104:4359–4364. [PubMed: 17360529]

Ward KM, Aletras AH, Balaban RS. A new class of contrast agents for MRI based on proton chemical exchange dependent saturation transfer (CEST). J Magn Reson 2000;143:79–87. [PubMed: 10698648]

Ward KM, Balaban RS. Determination of pH using water protons and chemical exchange dependent saturation transfer (CEST). Magn Reson Med 2000;44:799–802. [PubMed: 11064415]

Wijnen JP, van Asten JJ, Klomp DW, Sjobakk TE, Gribbestad IS, Scheenen TW, Heerschap A. Short echo time 1H MRSI of the human brain at 3T with adiabatic slice-selective refocusing pulses; reproducibility and variance in a dual center setting. J Magn Reson Imaging 31:61–70. [PubMed: 20027568]

Woessner DE, Zhang S, Merritt ME, Sherry AD. Numerical solution of the Bloch equations provides insights into the optimum design of PARACEST agents for MRI. Magn Reson Med 2005;53:790–799. [PubMed: 15799055]

Zhou J, Payen JF, Wilson DA, Traystman RJ, van Zijl PC. Using the amide proton signals of intracellular proteins and peptides to detect pH effects in MRI. Nat Med 2003;9:1085–1090. [PubMed: 12872167]

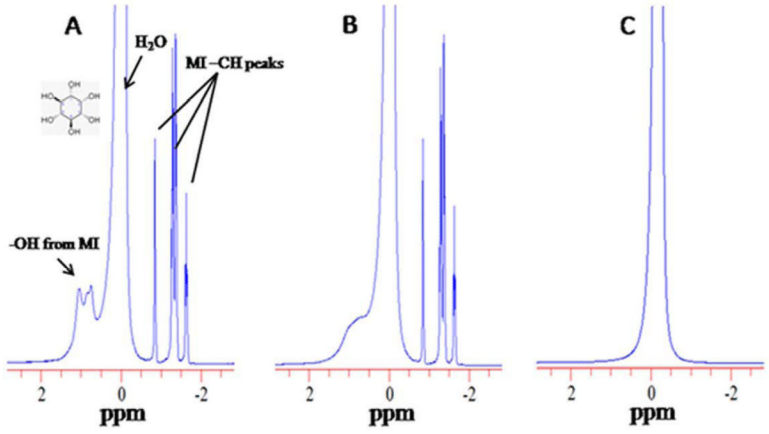

Figure 1.

The ^{1}H spectrum of 200mM MI. (A) showing the three –OH peaks downfield to bulk water proton resonance. Resonances from –CH groups are shown up field from water. The inset shows the chemical structure of MI. (B) The MI spectrum at pH 7.0 shows MI –CH resonances as well as broad –OH resonance. (C) Spectrum from PBS alone.

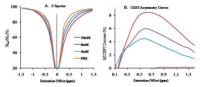

Figure 2.

(A) Z spectra of MI at different concentrations (pH7.4) are showing asymmetry due to the CEST effect from exchangeable –OH protons of MI. (B) CEST asymmetry curves shows the CEST effect centered ~0.6ppm from the bulk water resonance.

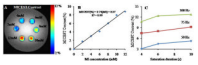

Figure 3.

A two-chamber phantom containing different concentrations of MI (2, 4, 6, 8, 10 and 12mM, pH 7.4) in the inner chamber and PBS in the outer chamber. Images were collected with a Hanning windowed saturation pulse of 6s duration and 75 Hz amplitude that was frequency selected at ±0.6ppm. Subtraction of the two images shows CEST contrast only from MI. (A) The MI signal overlay on the CEST image obtained at −0.6ppm. (B) Shows the linear dependence of MICEST effect on MI concentration with a slope of 0.74% per mM MI. (C) Depicts the changes in MICEST contrast with varying $B_1$and saturation pulse duration. The colorbar shows the MICEST contrast in percentage.

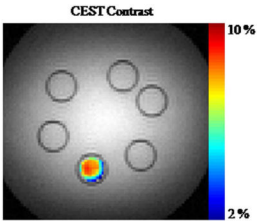

Figure 4.

Phantom consisting of test tubes with solution of different metabolites at their physiological concentrations [glucose (3mM), glycogen (3mM), Glu (10mM), Creatine (10mM), GABA (2mM), and MI (10mM), pH=7.4] immersed in a beaker containing PBS. Only MI shows predominant CEST contrast and negligible contributions from other metabolites. The colorbar shows the MICEST contrast in percentage.

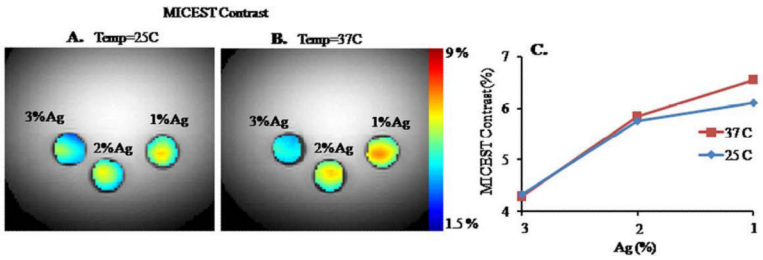

Figure 5.

MICEST maps of phantom consisting of test tubes with the same concentration of MI (10mM) in different viscous media (1%, 2% and 3% agarose). The highest MICEST contrast was observed in 1% agarose medium followed by 2% and 3% at both 25°C and 37°C (A and B). (C) Shows the higher MICEST contrast in 1% agarose at 37 °C compared to 25°C. The colorbar shows the MICEST contrast in percentage.

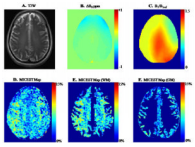

Figure 6.
Axial images of healthy human brain. (A) shows the T2 weighted image and figures B and C represent the corresponding B_0 and B_1 maps of the same slice. Figure D shows MICEST map from an axial slice of human brain. Figures E and F show the CEST maps from segmented white and gray matter regions, respectively.

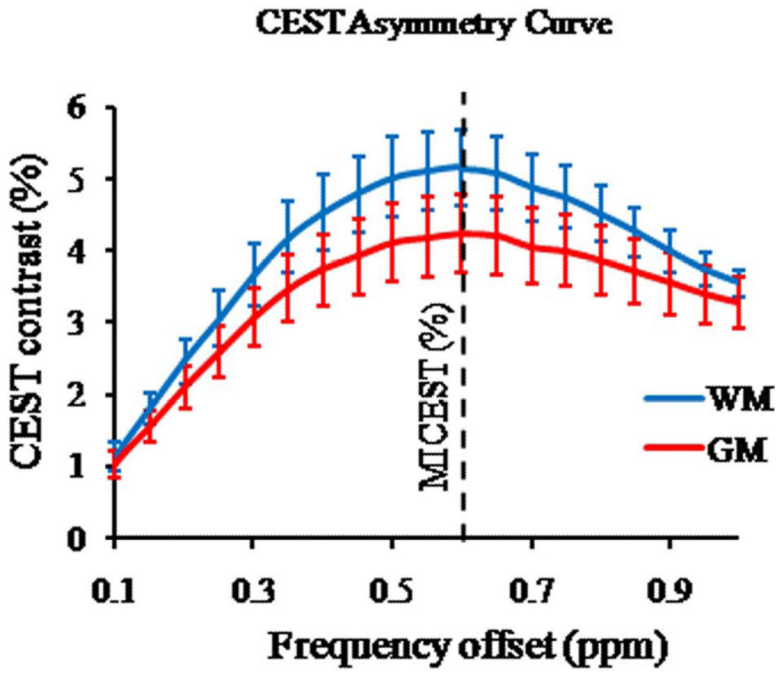

Figure 7.
The CEST asymmetric curves from the segmented white matter (WM) and gray matter (GM) regions of the brain. The dotted vertical line shows the peak of the MICEST at 0.6ppm.

Table 1

shows the average MICEST contrast as well as coefficient of variation (CV) in white matter (WM) and gray matter (GM) of five normal volunteers.

	MICEST (Mean)		CV	
Subject	**WM**	**GM**	**WM**	**GM**
1	4.93	4.06	0.49	0.52
2	5.47	4.95	0.51	0.69
3	5.71	4.48	0.49	0.60
4	4.33	3.47	0.55	0.60
5	5.34	4.29	0.43	0.48